

An implicit adaptive unified gas-kinetic scheme for steady-state solutions of non-equilibrium flows

Wenpei Long^a, Yufeng Wei^a, Kun Xu^{a,b,c,*}

^a*Department of Mathematics, Hong Kong University of Science and Technology, Hong Kong, China*

^b*Department of Mechanical and Aerospace Engineering, Hong Kong University of Science and Technology, Hong Kong, China*

^c*HKUST Shenzhen Research Institute, Shenzhen, 518057, China*

Abstract

In recent years, non-equilibrium flows have been frequently encountered in various aerospace engineering and micro-electro-mechanical systems applications. Numerical simulations enable us to understand non-equilibrium physics, multiscale effects, and the dynamics in these applications, which require an effective and reliable multiscale scheme for all flow regimes. Following the direct modeling methodology, the adaptive unified gas-kinetic scheme employs discrete velocity space to accurately capture the non-equilibrium physics, recovering the original unified gas-kinetic scheme (UGKS). Additionally, it adaptively employs continuous distribution functions based on the Chapman–Enskog expansion to efficiently achieve near-equilibrium flow regions with the gas-kinetic scheme (GKS). The UGKS and GKS are dynamically coupled at the cell interface through the fluxes from the discrete and continuous gas distribution functions, thereby avoiding any buffer zone between them. In the current study, an implicit adaptive unified gas-kinetic scheme (IAUGKS) is constructed to further enhance the efficiency of steady-state solutions. To preserve the capability for all flow regimes, a physical time step is introduced to determine the flow scale, while a numerical time step controls the time iteration. The current scheme employs implicit macroscopic governing equations and couples them with implicit microscopic governing equations within the non-equilibrium region, resulting in high convergence efficiency in all flow regimes. The point relaxation scheme is used to solve the implicit governing equations. To validate the efficiency and robustness of the IAUGKS, a series of numerical tests were conducted for high Mach number flows around diverse geometries such as a two-dimensional cylinder, a three-dimensional sphere, an X-38-like vehicle, and a space station. The current scheme can capture the non-equilibrium physics and provide accurate predictions of surface quantities. In comparison with the original UGKS, the velocity space adaptation, unstructured discrete velocity space (DVS), and implicit iteration significantly improve the efficiency by one or two orders of magnitude. Given its exceptional efficiency and accuracy, the IAUGKS serves as an effective tool for non-equilibrium flow simulations.

Keywords: Unified gas-kinetic scheme, Adaptive velocity space, Non-equilibrium flow, Implicit scheme

*Corresponding author.

Email address: makxu@ust.hk (Kun Xu)

1. Introduction

Non-equilibrium flow plays a critical role in aerospace engineering [1]. During the re-entry process of spacecraft, the atmospheric environment undergoes dramatic changes across multiple flow regimes from rarefied regime to continuum flow regime [2]. In hypersonic flows, non-equilibrium flow exists in different parts of the spacecraft [3], even though the Knudsen number of the incoming flow is relatively small. Traditional computational fluid dynamics methods, based on the continuity assumption, fail to capture these non-equilibrium flow physics. Consequently, the development of efficient and accurate multiscale simulation methods is of great importance.

To solve non-equilibrium flows, mainstream computational methods can be divided into two categories: stochastic and deterministic methods. Among stochastic methods, the direct simulation Monte Carlo (DSMC) [4–6] method is the most popular, which uses probabilistic Monte Carlo simulation to solve the Boltzmann equation, providing efficient and accurate results in rarefied flow regimes. Deterministic methods like the discrete velocity method (DVM) [7–10] or the discrete ordinate method (DOM) use the discrete velocity distribution function to solve the Boltzmann equation with different models. However, the computational efficiency of the DSMC method and the DVM decreases in continuum flow regimes due to the decoupling of particle collision and transport processes, limiting the time step and grid size to the scale of mean collision time and mean free path scale respectively.

Several explorations were made for deterministic methods to overcome the efficiency shortage of the conventional DVM in multiscale flows. Based on the direct modeling methodology [11], the unified gas-kinetic scheme (UGKS) [12] was proposed as a genuine multiscale method for all flow regimes. Under the framework of the finite volume method, the UGKS locally solves the Boltzmann equation with the Bhatnagar–Gross–Krook (BGK) [13] model when constructing the cell interface flux, thereby coupling the collision and free transport processes and breaking the time step limitation of the traditional DVM. In recent years, a series of multiscale methods based on the methodology of the DVM have emerged. Among them, the discrete unified gas-kinetic scheme (DUGKS) [14, 15] overcomes many shortages of the lattice Boltzmann equation method [16], and simplifies the UGKS, making the scheme easy to be implemented. Based on the traditional DVM, the improved DVM [17] and a variant of the improved DVM [18] were further developed. These methods use weighted coefficients to couple the near-continuous distribution function and discrete distribution function, breaking the limitation on time step and grid size of the original DVM. A rapidly converging general synthetic iterative scheme (GSIS) was proposed [19–21] by coupling the kinetic equation and its moment equations, while maintaining the ability to capture non-equilibrium physics. However, all methods mentioned above require discretizing the gas distribution function on a velocity space mesh, thus dramatically increasing the computational cost and memory consumption. In three-dimensional hypersonic flows, a large discrete velocity space (DVS) is needed to obtain accurate results, which consumes a significant amount of memory resources and slows down computational efficiency.

Multiscale stochastic methods that use statistical particles to describe distribution functions have also made significant progress. A unified gas-kinetic wave-particle (UGKWP) method [22, 23] was developed. This method replaces the DVS in the UGKS with stochastic particles, overcoming the substantial computational load and memory consumption of the UGKS, while maintaining its advantage of large time steps and grid sizes in the continuum flow regime. By using a wave-particle formulation, the UGKWP method substantially reduces the number of simulation particles

in near-continuum flow regime. The method has shown great performance in hypersonic non-equilibrium flows [24, 25], and has been extended to diatomic gas with rotational and vibrational non-equilibrium [26], plasma [27], photon transport [28], and multiphase flow problems [29–32]. In addition, based on the stochastic particle BGK method [33], the unified stochastic particle method [34, 35] is proposed. This method couples molecular motion and collision effects, overcoming the shortcoming of short time steps. A multi-scale Boltzmann equation method [36] was developed by coupling the DSMC method and NS solver directly and simply, and is validated in various cases. However, all stochastic methods face several challenges: In low-speed flows, the statistical noise contaminates the simulation result, leading to the use of a great number of particles and a long averaging process to get smooth results. Moreover, stochastic methods have difficulties when implementing acceleration techniques such as implicit iteration, resulting in slow convergence in steady-state solutions.

Given the above issues, research into acceleration and reducing memory consumption of deterministic methods is urgently needed. The implicit UGKS was proposed for both steady [37] and unsteady [38] solutions. By combining macroscopic prediction and microscopic implicit iteration, it achieves convergence 1 to 2 orders of magnitude faster than explicit UGKS in all flow regimes. The IUGKS was extended to three-dimensional thermal non-equilibrium flows [39], involving rotational and vibrational degrees of freedom. An implicit DUGKS [40] was also developed. Based on the traditional semi-implicit DVM, a fully implicit improved DVM [41] was proposed. In addition, A new implicit scheme [42] covering various flow regimes that directly solves the unified Boltzmann model equation was developed based on the gas-kinetic unified algorithm [43, 44]. However, due to the explicit handling of the equilibrium distribution function, the convergence efficiency is reduced. In terms of memory reduction techniques of the DVM, an unstructured DVS [45] was introduced, which significantly reduces the velocity space mesh in three-dimensional problems without affecting the accuracy of the results. The adaptive UGKS (AUGKS) [46] adopts a adaptive velocity space decomposition to capture the non-equilibrium part of the flow field, and use the discrete distribution function in the corresponding area and the continuous distribution function in other areas, saving memory consumption in the near-continuous flow regime. The effectiveness of the AUGKS in three-dimensional flows with rotational and vibrational non-equilibrium [47] was further proved. In addition, an adaptive DUGKS [48] and an adaptive UGKWP method [49] were proposed.

Considering the efficiency requirement in multiscale flows and the accuracy to capture non-equilibrium physics in engineering problems, an implicit adaptive unified gas-kinetic scheme is developed. This scheme significantly reduces memory consumption compared to the original UGKS and improves the convergence speed by one to two orders of magnitude in all flow regimes. Simultaneously, the IAUGKS retains the ability of the UGKS to capture non-equilibrium physics. It can effectively predict the heat flux, pressure, and shear stress on the surface of spacecraft, with results consistent with the UGKS or the DSMC data. Combining these properties, this scheme can provide effective and rapid simulation results in aerospace engineering, MEMS systems, and various other practical application fields.

The organization of this paper is as follows: in section 2, we introduce the general framework of the IAUGKS, along with its implicit iteration and velocity space adaptation. Section 3 validates the efficiency and accuracy of the current scheme by applying it to non-equilibrium flows, specifically, hypersonic flow around a cylinder, a sphere, an X-38 like vehicle, and a space station. The efficiency of the IAUGKS is compared with the original UGKS, the UGKWP method, and the GSIS, while

the accuracy of surface quantities is validated by the UGKS and DSMC data. Finally, Section 4 concludes the paper and outlines potential future work.

2. Numerical method

The IAUGKS adopts discrete and continuous velocity space adaptively for each region, thereby maintaining the ability to capture non-equilibrium physics and perform efficient computation simultaneously. The macroscopic implicit prediction is applied to the whole domain, and the microscopic implicit iterative update is used for the non-equilibrium region. In this section, the IUGKS is introduced first, including the macroscopic implicit prediction and microscopic implicit evolution. The IAUGKS is further demonstrated by introducing the treatment in near-continuum flow region and the velocity space adaptation at the interface of the discrete and continuous velocity space regions.

2.1. Implicit unified gas-kinetic scheme for steady-state solutions

In the current study, the BGK model is considered for the collision term in the Boltzmann Equation

$$\frac{\partial f}{\partial t} + u \frac{\partial f}{\partial x} = \frac{g - f}{\tau}. \quad (1)$$

Under the framework of the finite volume method, the implicit evolution of gas distribution function $f_{i,k}$ at the discrete velocity \mathbf{u}_k with backward Euler method is

$$f_{i,k}^{n+1} = f_{i,k}^n - \frac{\Delta t}{\Omega_i} \sum_{j \in N(i)} \mathcal{F}_{ij,k}^{n+1} \mathcal{A}_{ij} + \frac{\Delta t}{\tau_i^{n+1}} (g_{i,k}^{n+1} - f_{i,k}^{n+1}), \quad (2)$$

where the equilibrium gas distribution function $g_{i,k}^{n+1}$ and relaxation time τ_i^{n+1} are calculated from the macroscopic variables $\tilde{\mathbf{W}}_i^{n+1}$ given by macroscopic implicit prediction as

$$\tilde{\mathbf{W}}_i^{n+1} = \mathbf{W}_i^n - \frac{\Delta t}{\Omega_i} \sum_{j \in N(i)} \mathbf{F}_{ij}^{n+1} \mathcal{A}_{ij}. \quad (3)$$

The macroscopic variables at step $n + 1$ are provided by taking moments of the gas distribution function

$$\mathbf{W}_i^{n+1} = \sum_k f_{i,k} \boldsymbol{\psi}_k \mathcal{V}_k. \quad (4)$$

Therefore, the IUGKS mainly consists of two steps: macroscopic prediction and microscopic implicit iterative update.

2.2. Macroscopic implicit prediction

By subtracting the time-averaged flux \mathbf{F}_{ij}^n corresponding to the macroscopic variables at time step n from both sides of the macroscopic implicit prediction formula (3), we can rewrite it in the Δ form

$$\frac{\Omega_i}{\Delta t} \Delta \mathbf{W}_i + \sum_{j \in N(i)} \Delta \mathbf{F}_{ij} \mathcal{A}_{ij} = \mathbf{R}_i, \quad (5)$$

where $\Delta \mathbf{W}_i = \tilde{\mathbf{W}}_i^{n+1} - \mathbf{W}_i^n$ and $\Delta \mathbf{F}_{ij} = \mathbf{F}_{ij}^{n+1} - \mathbf{F}_{ij}^n$. \mathbf{R}_i is the residual

$$\mathbf{R}_i = - \sum_{j \in N(i)} \mathbf{F}_{ij}^n \mathcal{A}_{ij}. \quad (6)$$

For the UGKS, the macroscopic flux \mathbf{F}_{ij}^n is provided by taking moments of the time-averaged flux of the discrete gas distribution function

$$\mathbf{F}_{ij}^n = \sum_k \mathcal{F}_{ij,k}^n \boldsymbol{\psi}_k \mathcal{V}_k. \quad (7)$$

For steady-state solutions, the local time step Δt_{ij} at the interface is

$$\Delta t_{ij} = \min(\Delta t_i, \Delta t_j). \quad (8)$$

The time-averaged flux is expressed as

$$\mathcal{F}_{ij,k}^n = \frac{1}{\Delta t_{ij}} \int_0^{\Delta t_{ij}} \mathbf{u}_k \cdot \mathbf{n}_{ij} f_{ij,k}(t) dt, \quad (9)$$

where the time-dependent gas distribution function $f_{ij,k}(t)$ at the interface is modeled by the integral solution of the BGK Boltzmann equation along the characteristic line

$$f(\mathbf{r}, t) = \frac{1}{\tau} \int_0^t e^{-(t-t')/\tau} g(\mathbf{r}', t') dt' + e^{-t/\tau} f_0(\mathbf{r} - \mathbf{u}t), \quad (10)$$

where $\mathbf{r} - \mathbf{u}t$ denotes the trajectory of particles. The integral solution gives a multiscale modeling of an evolution process from an initial non-equilibrium distribution f to an equilibrium distribution g by collision. To achieve second-order accuracy, the initial and equilibrium distribution functions are constructed as

$$\begin{aligned} g_k(\mathbf{r}, t) &= g_{0,k} + \mathbf{r} \cdot \frac{\partial g_{0,k}}{\partial \mathbf{r}} + \frac{\partial g_{0,k}}{\partial t} t, \\ f_{0,k}(\mathbf{r}) &= f_k^{l,r} + \mathbf{r} \cdot \frac{\partial f_k^{l,r}}{\partial \mathbf{r}}, \end{aligned} \quad (11)$$

where $f_k^{l,r}$ is constructed by the initial distribution function interpolated to the left and right side of the interface

$$f_k^{l,r} = f_k^l H(\bar{u}_{ij,k}) + f_k^r [1 - H(\bar{u}_{ij,k})], \quad (12)$$

$H(\bar{u}_{ij,k})$ denotes the Heaviside step function, and $\bar{u}_{ij,k}$ is the particle velocity perpendicular to the interface. g_0 is the Maxwellian distribution function derived from the conservative variables contributed by all particles transported from both sides of the interface. Details of the distribution functions and derivatives are demonstrated in earlier work [11, 12].

By performing time integration, we have

$$\mathcal{F}_{ij,k}^n = \mathbf{u}_k \cdot \mathbf{n}_{ij} \left(L_1^u g_k^0 + L_2^u \mathbf{u}_k \cdot \frac{\partial g_k^0}{\partial \mathbf{x}} + L_3^u \frac{\partial g_k^0}{\partial t} + L_4^u f_k^{l,r} + L_5^u \mathbf{u}_k \cdot \frac{\partial f_k^{l,r}}{\partial \mathbf{x}} \right), \quad (13)$$

where L_1^u to L_5^u are time coefficients considering the local time step

$$\begin{aligned}
L_1^u &= 1 - \frac{\tau}{\Delta t_{ij}} (1 - e^{-\Delta t_{ij}/\tau}), \\
L_2^u &= -\tau + \frac{2\tau^2}{\Delta t_{ij}} - e^{-\Delta t_{ij}/\tau} \left(\frac{2\tau^2}{\Delta t_{ij}} + \tau \right), \\
L_3^u &= \frac{1}{2} \Delta t_{ij} - \tau + \frac{\tau^2}{\Delta t_{ij}} (1 - e^{-\Delta t_{ij}/\tau}), \\
L_4^u &= \frac{\tau}{\Delta t_{ij}} (1 - e^{-\Delta t_{ij}/\tau}), \\
L_5^u &= \tau e^{-\Delta t_{ij}/\tau} - \frac{\tau^2}{\Delta t_{ij}} (1 - e^{-\Delta t_{ij}/\tau}).
\end{aligned} \tag{14}$$

In addition, the macroscopic numerical flux corresponding to g_k^0 is directly given by the integration of the Maxwellian distribution function, which reduces the computational cost by summation.

The $\Delta \mathbf{F}_{ij}$ is approximated by flux vector splitting method as

$$\Delta \mathbf{F}_{ij} = \frac{1}{2} [\Delta \mathbf{T}_i + \Delta \mathbf{T}_j + \Gamma_{ij} (\Delta \mathbf{W}_i - \Delta \mathbf{W}_j)], \tag{15}$$

where $\Delta \mathbf{T}_i = \mathbf{T}_i^{n+1} - \mathbf{T}_i^n$. \mathbf{T} represents the Euler flux calculated from macroscopic variables by

$$\mathbf{T} = (\rho U_n, \rho \mathbf{U} U_n + p \mathbf{n}_{ij}, (\rho E + p) U_n)^T, \tag{16}$$

where $U_n = \mathbf{U} \cdot \mathbf{n}_{ij}$ denotes the component of macroscopic velocity \mathbf{U} in the interface normal direction \mathbf{n}_{ij} . Γ_{ij} represents the spectral radius of the Euler flux Jacobian matrix, and an additional stabilizing term related to kinetic viscosity is added considering the viscous effects

$$\Gamma_{ij} = |U_n| + a_s + \frac{2\mu}{\rho |\mathbf{n}_{ij} \cdot (\mathbf{x}_j - \mathbf{x}_i)|}, \tag{17}$$

where a_s is sound speed. By substituting the expression of $\Delta \mathbf{F}_{ij}$ in (15) into Eq. (5), and combining the fact that within a closed finite volume element \mathbf{T}_i satisfying

$$\sum_{j \in N(i)} \mathbf{T}_i \mathcal{A}_{ij} = \mathbf{0}, \tag{18}$$

the macroscopic governing equation is

$$\left(\frac{\Omega_i}{\Delta t} + \frac{1}{2} \sum_{j \in N(i)} \Gamma_{ij} \mathcal{A}_{ij} \right) \Delta \mathbf{W}_i + \frac{1}{2} \sum_{j \in N(i)} (\Delta \mathbf{T}_j - \Gamma_{ij} \Delta \mathbf{W}_j) \mathcal{A}_{ij} = - \sum_{j \in N(i)} \mathbf{F}_{ij}^n \mathcal{A}_{ij}, \tag{19}$$

where $\Delta \mathbf{T}_j$ can be obtained by the Jacobian matrix

$$\Delta \mathbf{T}_j = \left(\frac{\partial \mathbf{T}}{\partial \mathbf{W}} \right)_j \Delta \mathbf{W}_j. \tag{20}$$

In the current study, to avoid matrix operations, $\Delta \mathbf{T}_j$ can also use direct differential calculation

$$\Delta \mathbf{T}_j = \mathbf{T}(\mathbf{W}_j^n + \Delta \mathbf{W}_j) - \mathbf{T}(\mathbf{W}_j^n). \tag{21}$$

The point relaxation scheme is adopted to solve the macroscopic variables prediction equation. Instead of one forward-backward scanning process of the traditional lower-upper symmetric Gauss-Seidel (LU-SGS) method, the point relaxation scheme adopts multiple iteration steps. For the m th forward scanning process

$$\begin{aligned} & \left(\frac{\Omega_i}{\Delta t} + \frac{1}{2} \sum_{j \in N(i)} \Gamma_{ij} \mathcal{A}_{ij} \right) \Delta \mathbf{W}_i^* + \frac{1}{2} \sum_{j \in L(i)} \mathcal{A}_{ij} [\mathbf{T}(\mathbf{W}_j^n + \Delta \mathbf{W}_j^*) - \mathbf{T}(\mathbf{W}_j^n) - \Gamma_{ij} \Delta \mathbf{W}_j^*] \\ & + \frac{1}{2} \sum_{j \in U(i)} \mathcal{A}_{ij} [\mathbf{T}(\mathbf{W}_j^n + \Delta \mathbf{W}_j^{m-1}) - \mathbf{T}(\mathbf{W}_j^n) - \Gamma_{ij} \Delta \mathbf{W}_j^{m-1}] = \mathbf{R}_i, \end{aligned} \quad (22)$$

and the m th backward scanning process is

$$\begin{aligned} & \left(\frac{\Omega_i}{\Delta t} + \frac{1}{2} \sum_{j \in N(i)} \Gamma_{ij} \mathcal{A}_{ij} \right) \Delta \mathbf{W}_i^m + \frac{1}{2} \sum_{j \in L(i)} \mathcal{A}_{ij} [\mathbf{T}(\mathbf{W}_j^n + \Delta \mathbf{W}_j^*) - \mathbf{T}(\mathbf{W}_j^n) - \Gamma_{ij} \Delta \mathbf{W}_j^*] \\ & + \frac{1}{2} \sum_{j \in U(i)} \mathcal{A}_{ij} [\mathbf{T}(\mathbf{W}_j^n + \Delta \mathbf{W}_j^m) - \mathbf{T}(\mathbf{W}_j^n) - \Gamma_{ij} \Delta \mathbf{W}_j^m] = \mathbf{R}_i, \end{aligned} \quad (23)$$

where \mathbf{W}_j^{m-1} is the result of $m - 1$ th iteration and $\Delta \mathbf{W}_i^*$ is the result of m th forward scanning process.

2.2.1. Microscopic implicit iterative update

After the macroscopic implicit prediction, the equilibrium gas distribution function \tilde{g}^{n+1} and relaxation time $\tilde{\tau}^{n+1}$ at $n + 1$ step can be directly calculated from the predicted $\tilde{\mathbf{W}}^{n+1}$. By substituting \tilde{g}^{n+1} and $\tilde{\tau}^{n+1}$, and subtracting the time-averaged microscopic flux at n step, the delta-form of the microscopic implicit iteration equation is

$$\left(\frac{\Omega_i}{\Delta t} + \frac{\Omega_i}{\tilde{\tau}_i^{n+1}} \right) \Delta f_{i,k} + \sum_{j \in N(i)} \Delta \mathcal{F}_{ij,k} \mathcal{A}_{ij} = r_{i,k}, \quad (24)$$

where $r_{i,k}$ is the residual of discretized gas distribution function at \mathbf{u}_k

$$r_{i,k} = \frac{\Omega_i}{\tilde{\tau}_i^{n+1}} (\tilde{g}_{i,k}^{n+1} - f_{i,k}^n) - \sum_{j \in N(i)} \mathcal{F}_{ij,k}^n \mathcal{A}_{ij}. \quad (25)$$

For microscopic distribution function flux, a single first-order upwind scheme is adopted

$$\Delta \mathcal{F}_{ij,k} = u_{k,n} \{ H(u_{k,n}) \Delta f_{i,k} + [1 - H(u_{k,n})] \Delta f_{j,k} \}. \quad (26)$$

By substituting the microscopic distribution function flux (26) into the implicit governing equation (24), we have

$$D_{i,k} \Delta f_{i,k} + \sum_{j \in N(i)} D_{j,k} \Delta f_{j,k} = r_{i,k}, \quad (27)$$

where

$$D_{i,k} = \frac{\Omega_i}{\Delta t} + \frac{\Omega_i}{\tilde{\tau}_i^{n+1}} + \sum_{j \in N(i)} u_{k,n} \mathcal{A}_{ij} H(u_{k,n}), \quad (28)$$

$$D_{j,k} = u_{k,n} \mathcal{A}_{ij} [1 - H(u_{k,n})].$$

The microscopic implicit equation adopts traditional the LU-SGS method to decompose the process into a forward scanning process

$$D_{i,k} \Delta f_{i,k}^* + \sum_{j \in L(i)} D_{j,k} \Delta f_{j,k}^* + \sum_{j \in U(i)} D_{j,k} \Delta f_{j,k}^n = r_{i,k}, \quad (29)$$

and a backward scanning process

$$D_{i,k} \Delta f_{i,k}^{n+1} + \sum_{j \in L(i)} D_{j,k} \Delta f_{j,k}^* + \sum_{j \in U(i)} D_{j,k} \Delta f_{j,k}^{n+1} = r_{i,k}. \quad (30)$$

2.3. Implicit adaptive unified gas-kinetic scheme

In the near-continuum flow region, giving the validity of the Chapman–Enskog expansion, the IAUGKS adopts continuous gas distribution functions to reduce memory consumption and computational cost. The criterion for velocity space adaptation is given by the gradient-length local Knudsen number

$$\text{Kn}_{GU} = \frac{l}{\rho/|\nabla\rho|}, \quad (31)$$

where l is the local mean free path of gas molecules. When the Kn_{GU} is less than the given switching criterion C_t , the flow region is considered as near-continuum, thus the continuous gas distribution function is adopted; otherwise, the discretized gas distribution function is employed.

The treatment of the evolution in near-continuum flow regions is simplified as

$$\mathbf{W}_i^{n+1} = \tilde{\mathbf{W}}_i^{n+1}. \quad (32)$$

Instead of the summation over the whole discrete velocity space, the flux at the interface can be directly constructed from the continuous distribution function

$$\mathbf{F}_{ij}^n = \int \mathcal{F}_{ij} \psi d\mathbf{u}, \quad (33)$$

where \mathcal{F}_{ij} is a time-averaged flux constructed by a continuous distribution function the same as Eq (10). To capture the near-continuum flow physics and achieve second-order accuracy, the distribution functions are obtained by the Chapman–Enskog and Taylor expansion as

$$g(\mathbf{r}, t) = g_0 + \mathbf{r} \cdot \frac{\partial g_0}{\partial \mathbf{r}} + \frac{\partial g_0}{\partial t} t, \quad (34)$$

$$f_0(\mathbf{r}) = g^{l,r} - \tau \left(\mathbf{u} \cdot \frac{\partial g^{l,r}}{\partial \mathbf{r}} + \frac{\partial g^{l,r}}{\partial t} \right) + \mathbf{r} \cdot \frac{\partial g^{l,r}}{\partial \mathbf{r}}.$$

The time integration of the distribution function as the same as the GKS at the interface

$$\begin{aligned}
\mathcal{F}_{ij}^n &= \frac{1}{\Delta t_{ij}} \int_0^{\Delta t_{ij}} \mathbf{u} \cdot \mathbf{n}_{ij} f_{ij}(t) dt \\
&= \mathbf{u} \cdot \mathbf{n}_{ij} \left(L_1^g g^0 + L_2^g \mathbf{u} \cdot \frac{\partial g^0}{\partial \mathbf{x}} + L_3^g \frac{\partial g^0}{\partial t} + L_4^g g^{l,r} + L_5^g \mathbf{u} \cdot \frac{\partial g^{l,r}}{\partial \mathbf{x}} + L_6^g \frac{\partial g^{l,r}}{\partial t} \right),
\end{aligned} \tag{35}$$

where L_1^g to L_6^g are time coefficients

$$\begin{aligned}
L_1^g &= 1 - \frac{\tau}{\Delta t_{ij}} (1 - e^{-\Delta t_{ij}/\tau}), \\
L_2^g &= -\tau + \frac{2\tau^2}{\Delta t_{ij}} - e^{-\Delta t_{ij}/\tau} \left(\frac{2\tau^2}{\Delta t_{ij}} + \tau \right), \\
L_3^g &= \frac{1}{2} \Delta t_{ij} - \tau + \frac{\tau^2}{\Delta t_{ij}} (1 - e^{-\Delta t_{ij}/\tau}), \\
L_4^g &= \frac{\tau}{\Delta t_{ij}} (1 - e^{-\Delta t_{ij}/\tau}), \\
L_5^g &= \tau e^{-\Delta t_{ij}/\tau} - \frac{2\tau^2}{\Delta t_{ij}} (1 - e^{-\Delta t_{ij}/\tau}), \\
L_6^g &= -\frac{\tau^2}{\Delta t_{ij}} (1 - e^{-\Delta t_{ij}/\tau}).
\end{aligned} \tag{36}$$

The details and validity of the GKS are demonstrated in the previous work [50].

At the interface of the discrete and continuous velocity space regions, the gas distribution function is a combination of continuous and discrete distribution functions in each cell. By performing integration on both sides of the interface, we have

$$\begin{aligned}
\mathcal{F}_{ij,k} &= u_{k,n} \left(L_1^g g_{0,k} + L_2^g \mathbf{u}_k \cdot \frac{\partial g_{t,k}}{\partial \mathbf{x}} + L_3^g \frac{\partial g_{t,k}}{\partial t} \right) \\
&\quad + u_{k,n} \left\{ \left(L_4^g g_k^l + L_5^g \mathbf{u}_k \cdot \frac{\partial g_k^l}{\partial \mathbf{x}} + L_6^g \frac{\partial g_k^l}{\partial t} \right) H(u_{k,n}) + \left(L_4^u f_k^r + L_5^u \mathbf{u}_k \cdot \frac{\partial f_k^r}{\partial \mathbf{x}} \right) [1 - H(u_{k,n})] \right\}.
\end{aligned} \tag{37}$$

In addition, the $\Delta f_{j,k}$ used in the microscopic implicit iteration process is required at the region interface. For simplicity, the value is approximated by Maxwellian distribution instead of Champann–Enskog expansion

$$\Delta f_{j,k} = g_{j,k}^{n+1} - g_{j,k}^n. \tag{38}$$

2.4. Summary of algorithm

Step 1 Calculate gradients of macroscopic variables, and obtain Kn_{GU} .

Step 2 Perform velocity adaptation. Decompose the physical domain into continuous (GKS) and discrete (UGKS) distribution function regions by comparing Kn_{GU} and given criterion C_t .

Step 3 Calculate the microscopic and macroscopic numerical flux on the cell interface.

Step 4 Evaluate the macroscopic residual \mathbf{R}_i .

- Step 5** Perform macroscopic implicit prediction using R_i with the point relaxation scheme.
- Step 6** Evaluate the microscopic residual $r_{i,k}$ in the discretized (UGKS) distribution function region using \tilde{g}^{n+1} and $\tilde{\tau}^{n+1}$ obtained in step 4.
- Step 7** Perform microscopic implicit iterative update using $r_{i,k}$ with the LUSGS method. Use the Maxwellian distribution function to obtain $\Delta f_{j,k}$ in adjacent GKS cells of UGKS cells.
- Step 8** Update macroscopic conservative variables. In near-continuum flow regions, the macroscopic variables are directly updated by implicit prediction; otherwise, the macroscopic variables are calculated by the summation of updated discretized distribution function $f_{j,k}^{n+1}$.

A concise schematic diagram of the velocity space adaptation and the iteration of the IAUGKS is plotted in Fig. 1.

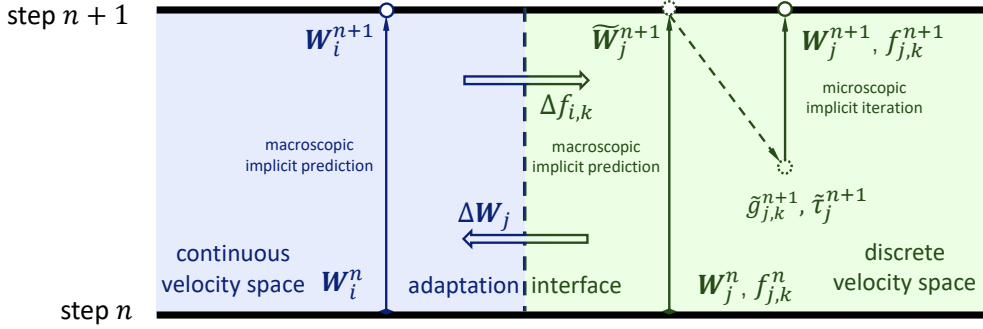


Figure 1: A schematic diagram of the IAUGKS. The figure demonstrates the iteration of the IAUGKS in different regions and the treatment at their interfaces.

3. Numerical Validation

3.1. Hypersonic flow around a circular cylinder

Hypersonic gas flow of nitrogen around a circular cylinder has been simulated at $Ma_\infty = 5$ and $Kn_\infty = 0.1$. The characteristic length used to define the Knudsen number is the cylinder diameter $D = 1$ m. The temperature of free stream flow is $T_\infty = 273$ K, and an isothermal wall with a fixed temperature of $T_w = 273$ K is applied for the cylinder surface. The physical domain is discretized by 5000 quadrilateral cells, while the unstructured discrete velocity space (DVS) mesh consists of 2,060 cells as shown in Fig. 2. The DVS is discretized in a circle region with the center $0.4 \times (U_\infty, V_\infty, W_\infty)$ with a total radius of $6\sqrt{RT_s}$ where T_s is the stagnation temperature of the free stream flow. The unstructured DVS mesh is refined at zero velocity point with a radius of $3\sqrt{RT_w}$, and the free stream velocity point with a radius of $3\sqrt{RT_\infty}$.

To validate the velocity space adaptation, cases with criteria of $C_t = 0.005$, $C_t = 0.01$, and $C_t = 0.05$ are simulated by the IAUGKS. The flow contours are plotted in Figures 3 to 5, where a tiny difference can be observed in the Mach number and temperature contour at the leeward region. Figure 7 shows the temperature distribution along the stagnation line. Compared with the explicit UGKS data, a deviation at the front of the shock region appears in $C_t = 0.05$ while other data all fit well. As depicted in Figure 8, the pressure and shear stress coefficients on the cylinder

surface are consistent for all criteria, but for $C_t = 0.05$ the heat flux coefficient at the windward region slightly deviates from the reference.

Figure 6 depicts that 59.83%, 55.01%, and 29.71% of the computational domain is covered by DVS (UGKS) for $C_t = 0.005$, $C_t = 0.01$, and $C_t = 0.05$ respectively. The physical CFL number is set to 0.4 and the numerical CFL number for implicit iteration is set to 400. As shown in Table 1, the simulation time decreases as the proportion of the DVS region shrinks. Compared with the original explicit UGKS, the unstructured DVS helps to improve the efficiency by 3 times; by adding the implicit algorithm, the simulation time further diminishes by nearly 100 times. Moreover, with different decomposition criterion, the computation efficiency of the IAUGKS is raised to over 700 times higher than the original UGKS with structured DVS. All the IAUGKS simulations are conducted on a personal computer with a single core of intel 13700K @5.30 GHz.

The cases with different decomposition criteria give reasonable results with different acceleration rates. Considering the ability to capture non-equilibrium physics and computation efficiency in conjunction, $C_t = 0.01$ and $C_t = 0.05$ are suitable for non-equilibrium flow simulations.

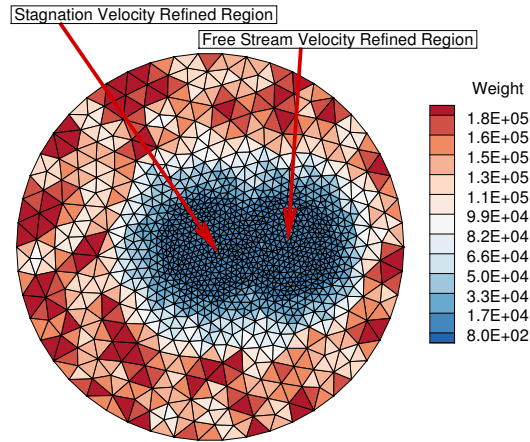


Figure 2: Unstructured DVS mesh used for hypersonic flow at $Kn = 0.1$ and $Ma = 5$ passing over a cylinder by the IAUGKS.

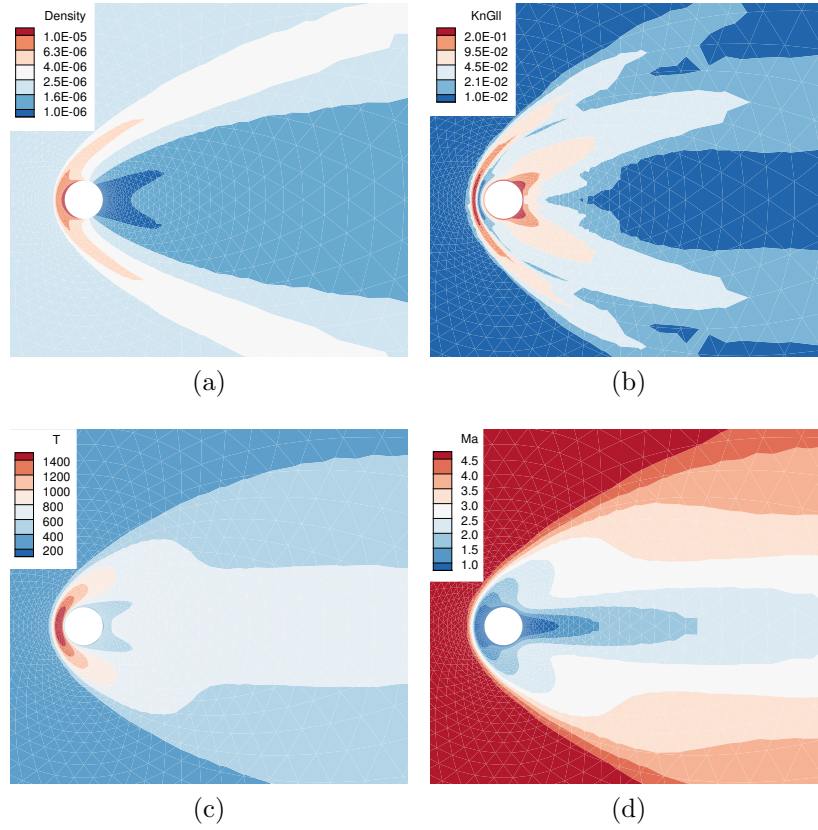


Figure 3: Hypersonic flow at $Kn = 0.1$ and $Ma = 5$ passing over a circular cylinder with $C_t = 0.005$ by the IAUGKS. (a) Density, (b) Kn_{GII} , (c) temperature, and (d) Mach number contours.

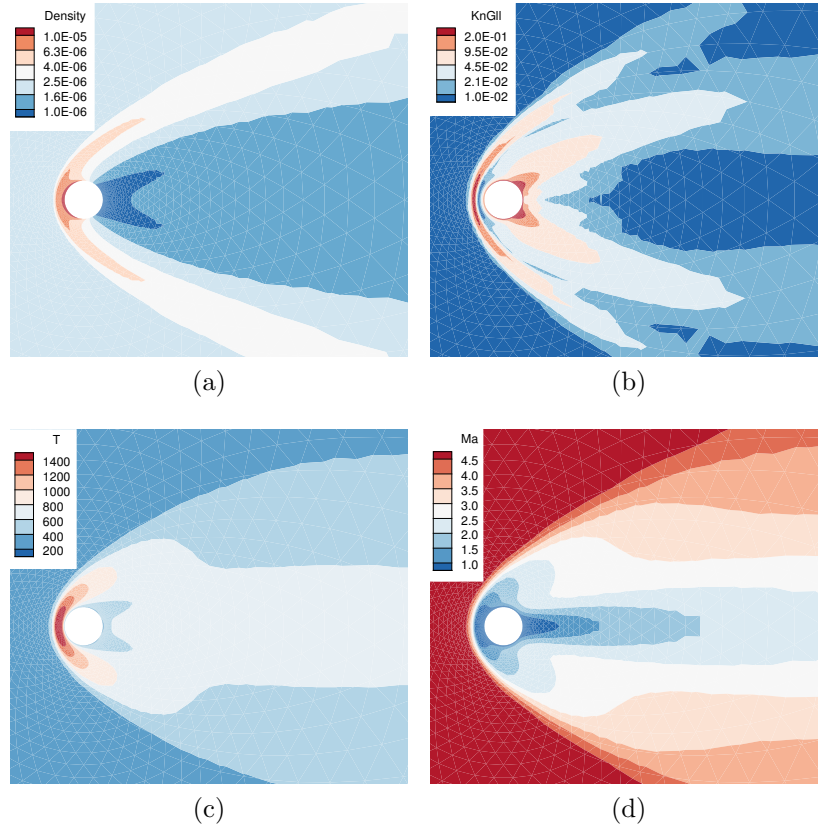


Figure 4: Hypersonic flow at $Kn = 0.1$ and $Ma = 5$ passing over a circular cylinder with $C_t = 0.01$ by the IAUGKS. (a) Density, (b) Kn_{GII} , (c) temperature, and (d) Mach number contours.

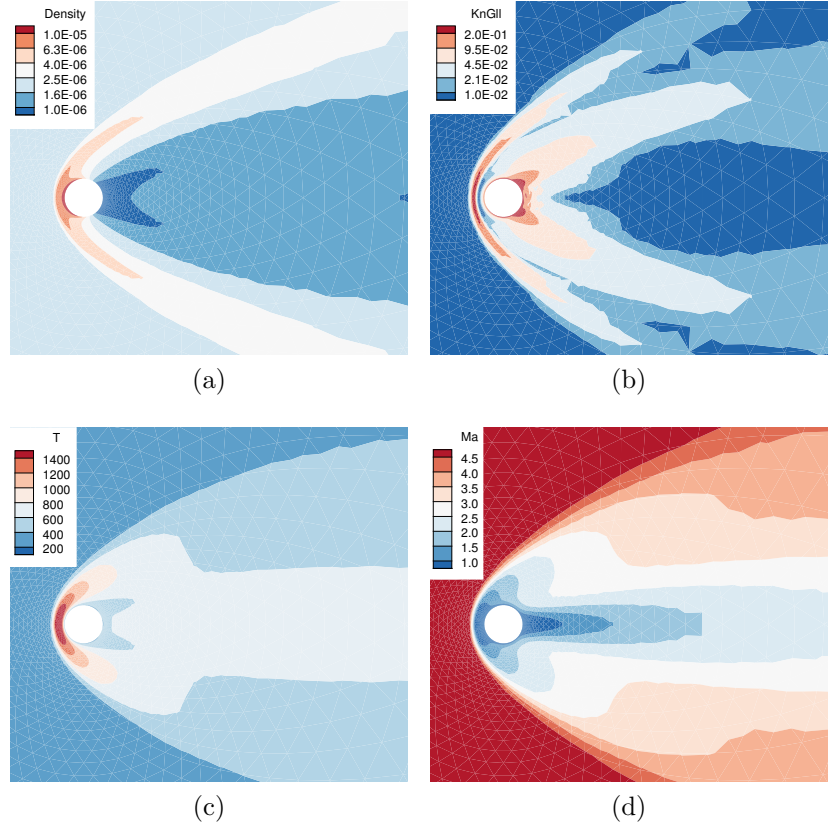


Figure 5: Hypersonic flow at $Kn = 0.1$ and $Ma = 5$ passing over a circular cylinder with $C_t = 0.05$ by the IAUGKS. (a) Density, (b) Kn_{GII} , (c) temperature, and (d) Mach number contours.

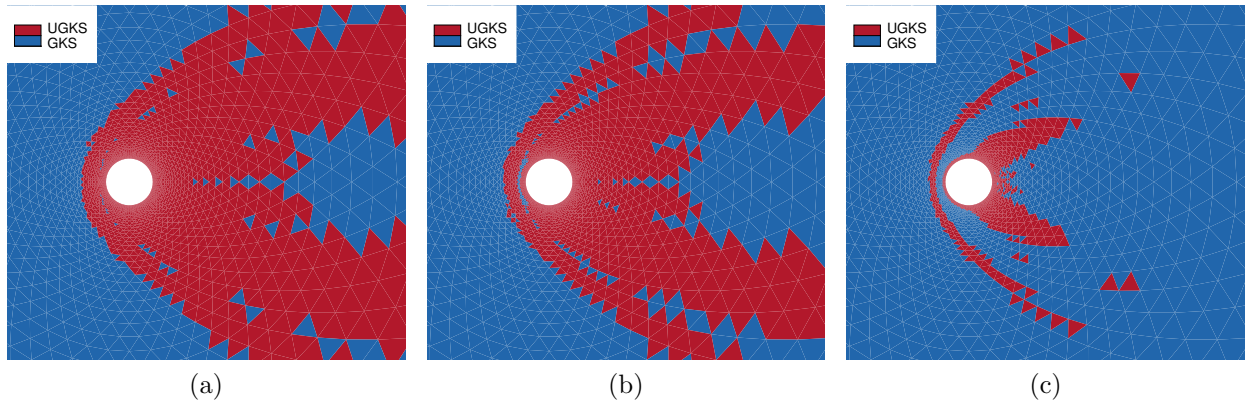
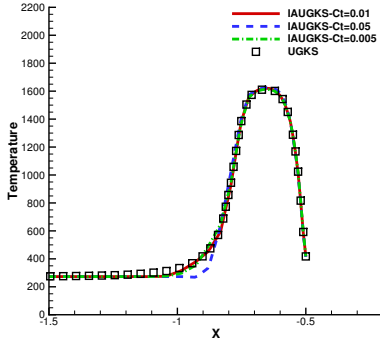
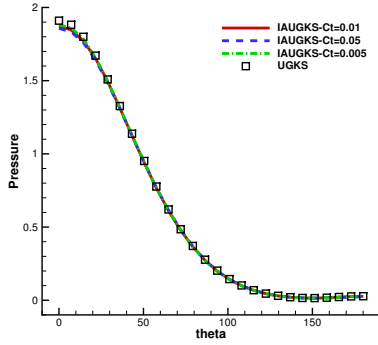


Figure 6: Hypersonic flow at $Kn = 0.1$ and $Ma = 5$ passing over a circular cylinder by the IAUGKS. Distributions of velocity space adaptation with (a) $C_t = 0.005$, (b) $C_t = 0.01$, and (c) $C_t = 0.05$.

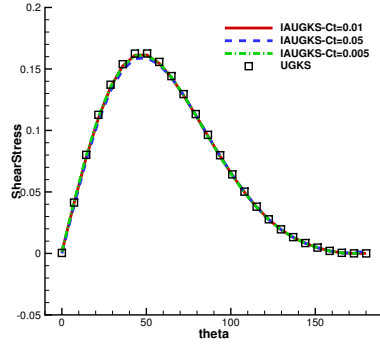


(a)

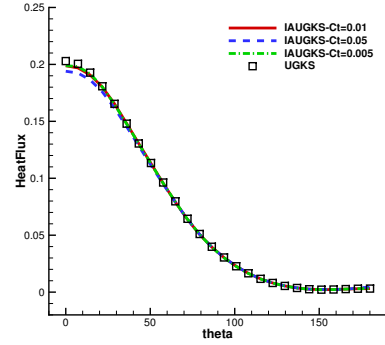
Figure 7: Hypersonic flow at $Kn_\infty = 0.1$ and $Ma = 5$ passing over a circular cylinder by the IAUGKS. The temperature distribution along the stagnation line.



(a)



(b)



(c)

Figure 8: Hypersonic flow at $Kn_\infty = 0.1$ and $Ma = 5$ passing over a circular cylinder by the IAUGKS. Surface quantities distributions: (a) pressure, (b) shear stress, and (c) heat flux.

Table 1: The computational cost for simulations of hypersonic flow at $\text{Kn}_\infty = 0.1$ and $\text{Ma} = 5$ around a cylinder by the IAUGKS. The physical domain consists of 5,000 cells, and the unstructured DVS mesh is discretized by 2,060 cells.

Solver	Acceleration Method	Steps	Simulation Time, h	Acceleration Rate
UGKS	Original UGKS	40000	190.7	1
UGKS	unstructured DVS	45000	63.3	3.01
UGKS	unstructured DVS implicit iteration	$1000^1 + 300$	0.665	286.8
UGKS	unstructured DVS implicit iteration Adaptation $C_t = 0.005$	$1000^1 + 300$	0.411	464.0
UGKS	unstructured DVS implicit iteration Adaptation $C_t = 0.01$	$1000^1 + 300$	0.379	503.2
UGKS	unstructured DVS implicit iteration Adaptation $C_t = 0.05$	$1000^1 + 300$	0.262	727.9

¹ Steps of first-order GKS simulations.

To further verify the computational accuracy and robustness of the current scheme, hypersonic flow passing over a circular cylinder at a very large Mach number $\text{Ma}_\infty = 15$ and $\text{Kn}_\infty = 0.01$ is simulated. The computation domain and geometry characteristics are the same as in the first case. The temperature in free stream flow is $T_\infty = 217.5$ K and the isothermal wall boundary is set to a fixed temperature of $T_w = 300$ K. Figure 9 shows the unstructured DVS mesh consists of 3,420 cells. The DVS is discretized in a circle region with the center $0.4 \times (U_\infty, V_\infty, W_\infty)$, and the radius is $5\sqrt{RT_s}$ where T_s is the stagnation temperature of the free stream flow. The unstructured DVS mesh is refined at zero velocity point with a radius of $5\sqrt{RT_w}$, and the free stream velocity point with a radius of $5\sqrt{RT_\infty}$.

The flow contours with $C_t = 0.01$ are plotted in Fig. 10. Figure 11 shows 25.12% of the region is covered by DVS with the current criterion. The vicinity of shock and leeward regions are contained within the UGKS region, which is consistent with the highly non-equilibrium area shown in the Kn_{GII} contour. Even though most of the computation domain is covered by the GKS, the IAUGKS gives accurate predictions of surface quantities compared with the explicit UGKS.

The physical CFL number is set to 0.4 and the numerical CFL number for implicit iteration is set to 40. The computation efficiency is compared with the original UGKS with structured DVS and the IUGKS. All the IAUGKS simulations are conducted on a personal computer platform with a single core of intel 13700K @5.30 GHz.

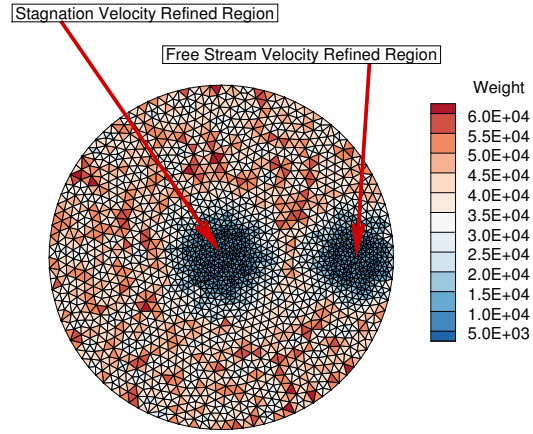


Figure 9: Unstructured DVS mesh used for hypersonic flow at $Kn = 0.01$ and $Ma = 15$ passing over a cylinder by the IAUGKS.

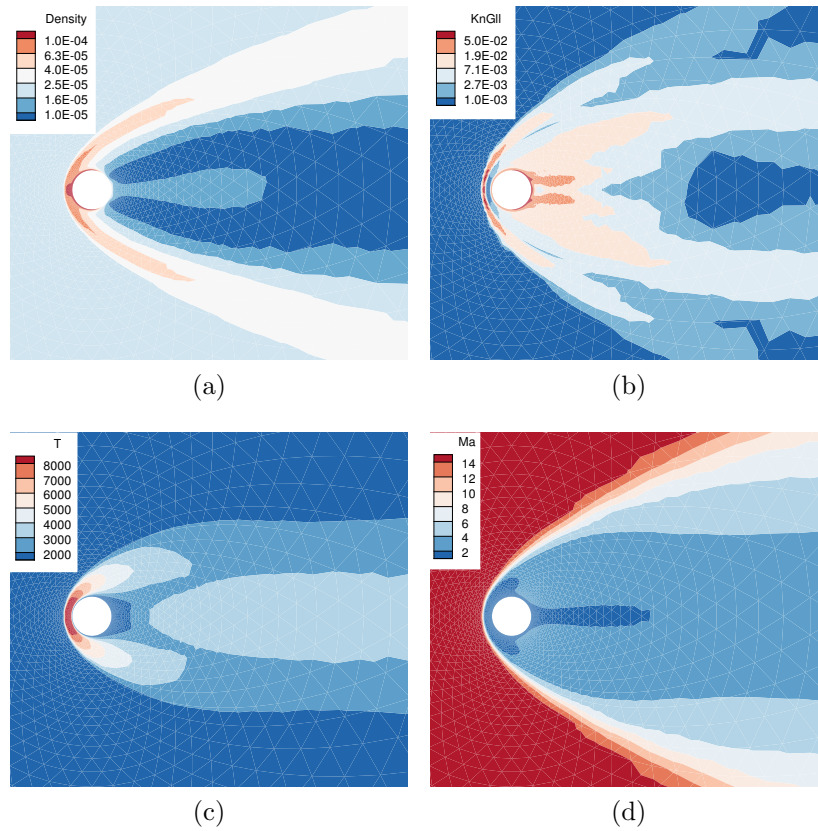
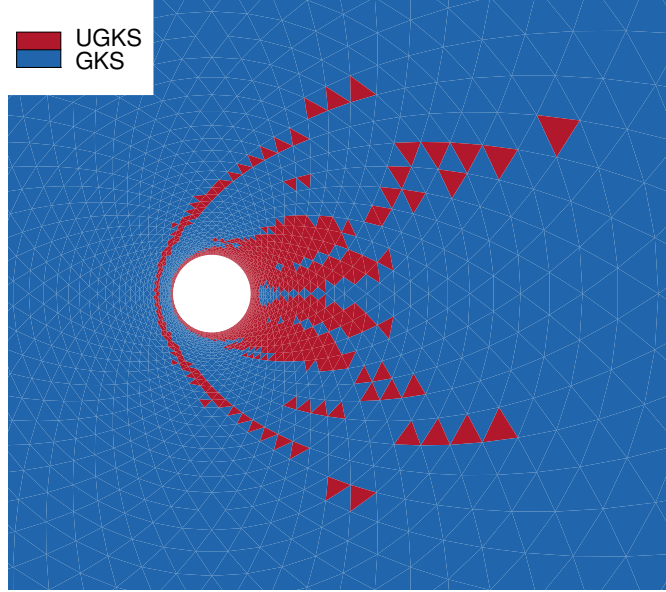
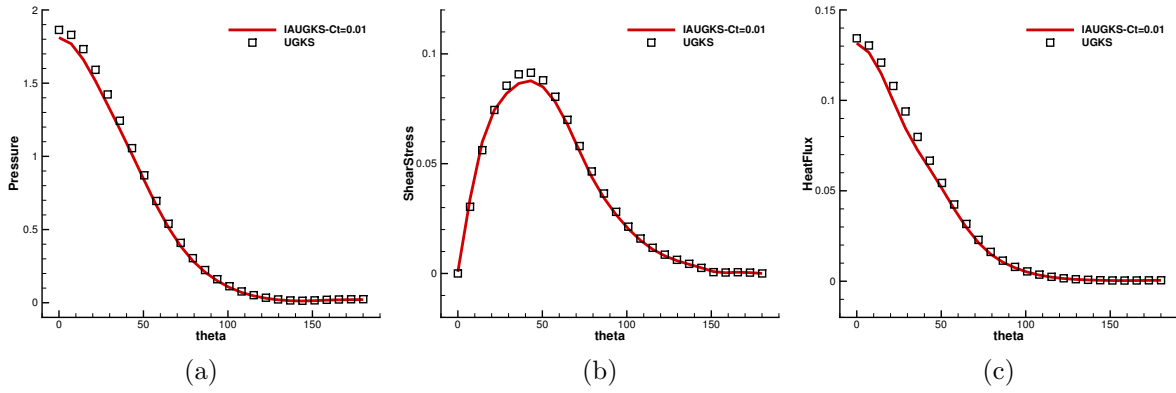


Figure 10: Hypersonic flow at $Kn = 0.01$ and $Ma = 15$ passing over a circular cylinder with $C_t = 0.01$ by the IAUGKS. (a) Density, (b) Kn_{GII} , (c) temperature, (d) Mach number contours.



(a)

Figure 11: Hypersonic flow at $Kn = 0.01$ and $Ma = 15$ passing over a circular cylinder by the IAUGKS. Distributions of velocity space adaptation with $C_t = 0.01$.



(a)

(b)

(c)

Figure 12: Hypersonic flow at $Kn_\infty = 0.01$ and $Ma = 15$ passing over a circular cylinder by the IAUGKS. Surface quantities distributions: (a) pressure, (b) shear stress, and (c) heat flux.

Table 2: The computational cost for simulations of hypersonic flow at $\text{Kn}_\infty = 0.01$ and $\text{Ma} = 15$ around a cylinder by the IAUGKS. The physical domain consists of 5,000 cells, and the unstructured DVS mesh is discretized by 3,420 cells.

Solver	Acceleration Method	Steps	Simulation Time, h	Acceleration Rate
UGKS	Original UGKS	$2600^1 + 12000$	340.1	1
UGKS	unstructured DVS	$2600^1 + 10000$	95.47	3.6
UGKS	unstructured DVS implicit iteration	$2600^1 + 300$	1.462	232.5
UGKS	unstructured DVS implicit iteration Adaptation $C_t = 0.01$	$2600^1 + 400$	0.432	786.4

¹ Step of first-order GKS simulations.

3.2. Supersonic flow around a sphere

To further verify the effectiveness and efficiency of the IAUGKS in three-dimensional cases, the supersonic flow passing over a sphere at Mach number 4.25 for $\text{Kn}_\infty = 0.031$ and $\text{Kn}_\infty = 0.0031$ are simulated for nitrogen gas. The characteristic length is chosen as the sphere diameter $D = 0.002$ m to define the Knudsen number. The physical domain contains $3,456 \times 40$ hexahedron cells, and the surface mesh is divided into 6 domains with 24×24 cells in each domain. Figure 13 illustrates the section view of unstructured DVS mesh with 18,802 cells. The DVS is discretized into a sphere mesh with a radius of $6\sqrt{RT_s}$. The sphere center is located at $0.4 \times (U_\infty, V_\infty, W_\infty)$, and the velocity space near the zero and free stream velocity point are refined within a spherical region of radius $r = 3\sqrt{RT_w}$ and $r = 3\sqrt{RT_\infty}$ respectively. Table 3 gives the initial conditions of free stream flow, i.e., ρ_∞ and T_∞ for different Kn_∞ , and the temperature of isothermal wall boundary condition T_w .

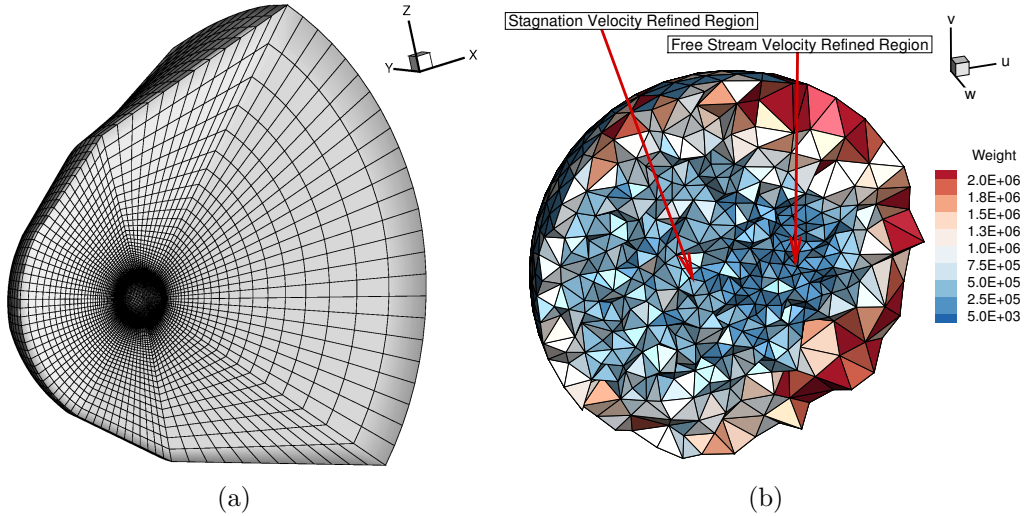


Figure 13: Supersonic flow at $\text{Ma}_\infty = 4.25$ passing over sphere by the IAUGKS. (a) Physical mesh consisting of 138,240 cells, and (b) unstructured DVS mesh consisting of 18,802 cells.

Table 3: Free stream flow parameters of supersonic flow at $Ma_\infty = 4.25$ around a sphere.

Kn_∞	Altitude, km	ρ_∞ , kg/(m ³ · s)	T_∞ , K	T_w , K
0.031	63.2	6.879×10^{-4}	65.04	302
0.0031	41.5	6.879×10^{-3}	65.04	302

Figures 15 and 16 depict the contours of density, gradient length local Knudsen number, Mach number, and temperature by the IAUGKS for different Kn_∞ . Figure 17 illustrates the domain decomposition with $C_t = 0.01$, where 63.87% and 36.96% region are covered by DVS for $Kn_\infty = 0.031$ and $Kn_\infty = 0.0031$ respectively.

The drag coefficients predicted by the IAUGKS are shown in Table 4. Compared with experiment data for Air [51] and UGKS data for nitrogen [52], the IAUGKS gives accurate results with errors as small as 1.91%. To further verify the ability to accurately predict surface quantities, the pressure, shear stress, and heat flux coefficient distribution are compared with the explicit UGKS for $Kn_\infty = 0.031$. The non-dimensionalized surface coefficients are given by

$$C_p = \frac{p_s - p_\infty}{\frac{1}{2}\rho_\infty U_\infty^2}, \quad C_\tau = \frac{f_s}{\frac{1}{2}\rho_\infty U_\infty^2}, \quad C_h = \frac{h_s}{\frac{1}{2}\rho_\infty U_\infty^3},$$

where velocity U_∞ can be calculated by free-stream Mach number Ma_∞ , p_s is the surface pressure, p_∞ is the pressure in free stream flow, f_s is the surface friction and h_s is the surface heat flux. For $C_t = 0.01$, the simulation results of the IAUGKS fit well with the explicit UGKS; for $C_t = 0.05$, the heat flux coefficient at the windward region deviates from the reference. For three-dimensional flows, the validity of the criterion is consistent with that of the two-dimensional flows.

Table 4: Drag coefficients of supersonic flow around a sphere at $Ma_\infty = 4.25$ by the IAUGKS.

Ma_∞	Kn_∞	Drag Coefficient (Error)		
		Experiment (Air)	UGKS (N ₂)	IAUGKS (N ₂)
4.25	0.031	1.35	1.355 (0.39%)	1.376 (1.91%)
4.25	0.0031	-	1.162 (-)	1.166 (-)

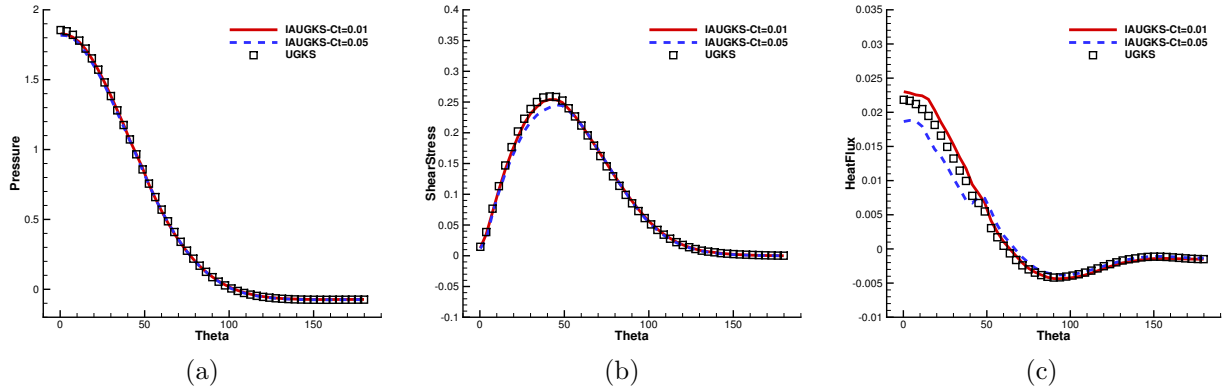


Figure 14: Surface quantities of supersonic flow around a sphere at $Ma_\infty = 4.25$ for $Kn_\infty = 0.031$ by the IAUGKS. (a) Pressure coefficient, (b) shear stress coefficient, and (c) heat flux coefficient.

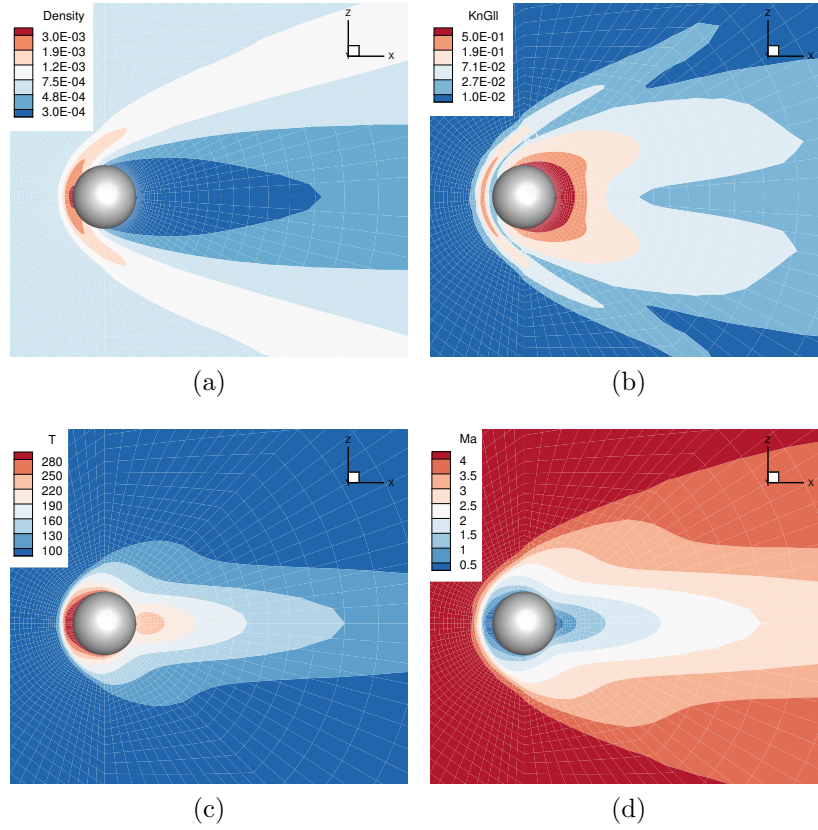


Figure 15: Supersonic flow around a sphere at $Ma_\infty = 4.25$ for $Kn_\infty = 0.031$ by the IAUGKS. (a) Density, (b) Kn_{GII} , (c) temperature, and (d) Mach number contours.

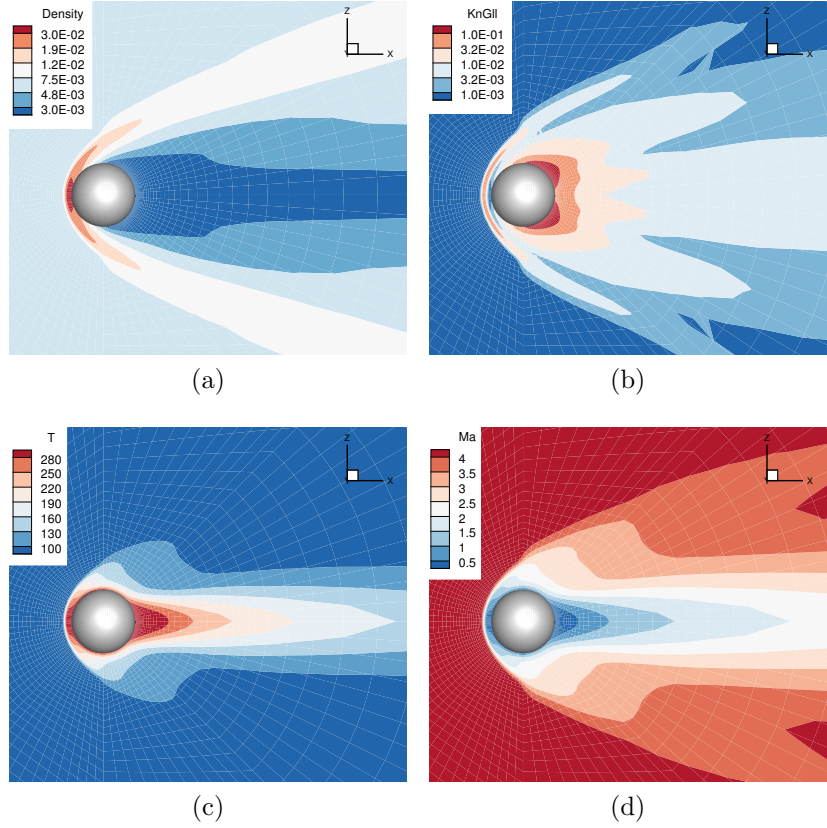


Figure 16: Supersonic flow around a sphere at $Ma_\infty = 4.25$ for $Kn_\infty = 0.0031$ by the IAUGKS. (a) Density, (b) Kn_{GII} , (c) temperature, and (d) Mach number contours.

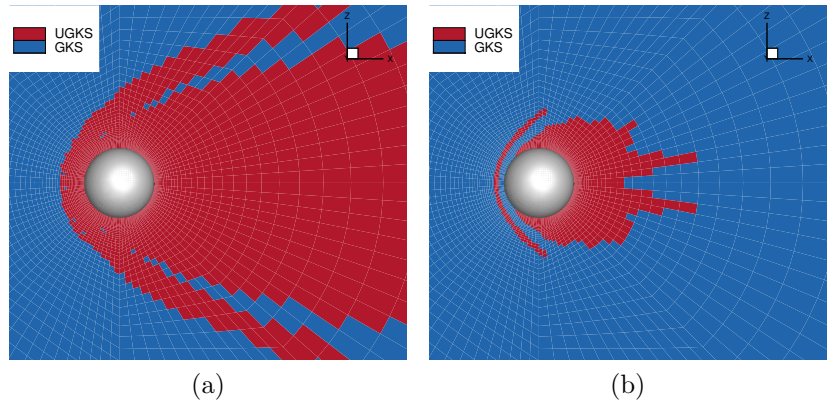


Figure 17: Supersonic flow around a sphere at $Ma_\infty = 4.25$ by the IAUGKS. Proportions of DVS with $C_t = 0.01$ for (a) $Kn_\infty = 0.031$ is 63.87%, and for (b) $Kn_\infty = 0.0031$ is 36.96%.

The physical CFL number is set to 0.4 and the numerical CFL number for implicit iteration is set to 400. Table 5 shows the computational efficiency and resource consumption for $Kn_\infty = 0.031$ and $Kn_\infty = 0.0031$. In three-dimensional cases, the implicit algorithm dramatically enhances the computational efficiency of the explicit AUGKS by nearly 26 times, achieving the same level of

efficiency as the UGKWP method. A simple static load balancing method is adopted. Fig. 18 shows that after the load balancing process, regions using DVS in Fig. 17 (a) are decomposed into more partitions. All the simulations are conducted on the SUGON computation platform with a CPU model of 7285 32C 2.0GHz.

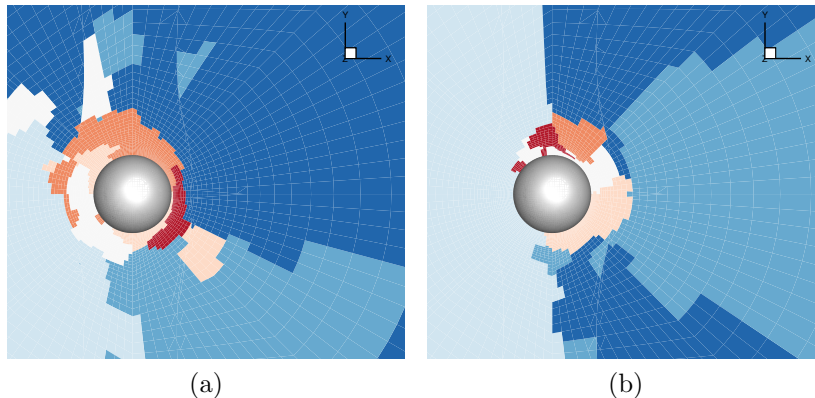


Figure 18: Supersonic flow around a sphere at $Ma_\infty = 4.25$ and $Kn_\infty = 0.031$ by the IAUGKS. The partitioning of the computation domain (a) before the load balancing, and (b) after the load balancing.

Table 5: The computational cost for simulations of the supersonic flow around a sphere at $Ma_\infty = 4.25$ by the IAUGKS. The physical domain consists of 138,240 cells, and the unstructured DVS mesh is discretized by 18,802 cells. The criterion of the velocity space adaptation is $C_t = 0.01$ for the IAUGKS and the AUGKS simulations.

Kn_∞	Method	Cores	Steps	Wall Clock Time, h
0.031	IAUGKS	640	3200 ¹ + 90	1.51
0.031	AUGKS	1920	4000 ¹ + 3500	9.97
0.031	UGKWP	128	12000 + 13000 ²	3.46
0.0031	IAUGKS	640	3400 ¹ + 100	0.416
0.0031	AUGKS	1920	2500 ¹ + 3100	7.96

¹ Steps of first-order GKS simulations.

² Average steps of UGKWP simulations.

3.3. Hypersonic flow around an X38-like space vehicle

In this section, hypersonic flow at $Ma_\infty = 8.0$ passing over an X38-like space vehicle for $Kn_\infty = 0.00275$ at angles of attack of $AoA = 20^\circ$ is simulated. The reference length to define the Knudsen number is $L_{ref} = 0.28$ m. In this case, due to the hypersonic free stream flow in the transition regime and the complex geometric shape, all flow regimes are involved, posing a great challenge to the numerical solver. The free stream temperature is $T_\infty = 56$ K, and an isothermal wall is applied to the vehicle surface with $T_w = 302$ K.

The physical mesh consists of 600,078 all kinds of cells with the cell height of the first layer mesh $h = 1.5 \times 10^{-4}$ m, as shown in Fig. 19. The unstructured DVS mesh is depicted in Fig. 20. The DVS is discretized into 23,520 cells in a sphere mesh with a radius of $5\sqrt{RT_s}$. The sphere center is located at $0.4 \times (U_\infty, V_\infty, W_\infty)$, the velocity space near the zero and free stream velocity point are refined within a spherical region of radius $r = 5\sqrt{RT_w}$ and $r = 5\sqrt{RT_\infty}$ respectively.

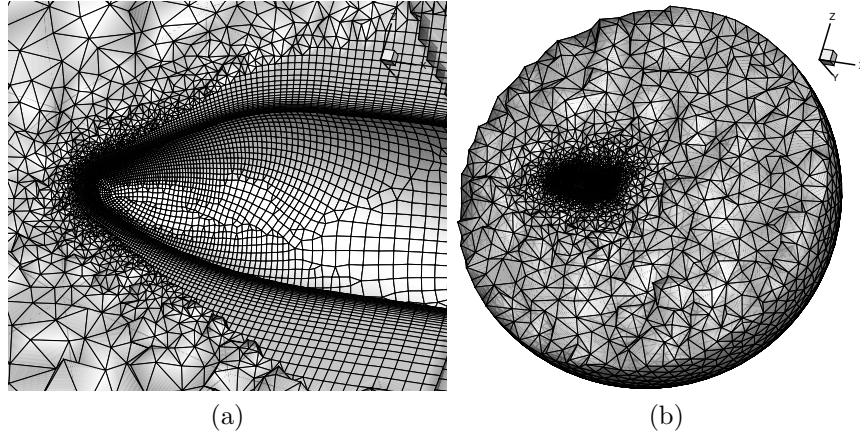


Figure 19: Section view of the physical mesh of the X38-like space vehicle with 600,078 cells: (a) close view of the vehicle nose, and (b) half of the domain.

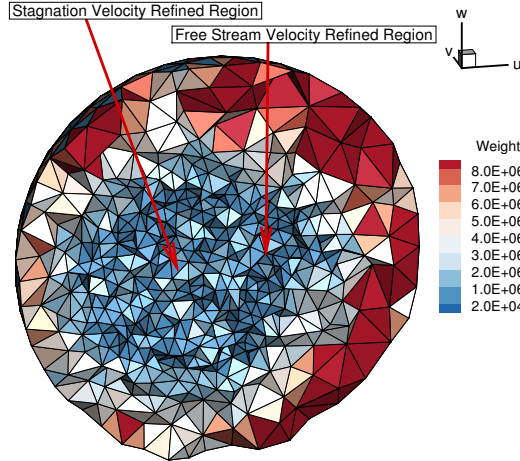


Figure 20: Unstructured DVS mesh with 23,520 cells used for hypersonic flow at $Ma_\infty = 8.0$ and $Kn_\infty = 0.00275$ passing over an X38-like space vehicle by the IAUGKS.

Figure 21 illustrates contours of the density, gradient-length local Knudsen number, temperature, and Mach number. Even though the free stream flow is in near continuum regime, the gradient-length local contour denotes strong non-equilibrium flow in the leeward region, where the Kn_{GII} is 4 to 5 orders of magnitude higher than in the free stream flow. Figure 22 shows that the velocity space adaptation mechanism successfully detects the non-equilibrium region and uses DVS for 46.37% of the whole computation domain.

Figure 23 depicts the surface quantities on the symmetric cross-section perpendicular to the y -axis and comparisons with the DSMC data. All coefficients predicted by the IAUGKS with $C_t = 0.05$ align well with the DSMC reference. However, if continuous velocity space is applied for the whole computation domain, the IGKS gives false result in terms of shear stress and heat flux at the leeward region and the forebody of the vehicle. This also implies strong non-equilibrium effect exists within these regions, which cannot be captured by the traditional continuum solver. This shows the importance of the velocity space adaptation.

The simulation takes 35,000 steps of the GKS and 250 steps of the IAUGKS, and the physical CFL number is set to 0.4 and the numerical CFL number for implicit iteration is set to 100. A simple static load balancing method is adopted. The simulation is conducted on the SUGON computation platform which takes 4.86 hours of wall clock time on 640 cores of CPU 7285 32C 2.0GHz.

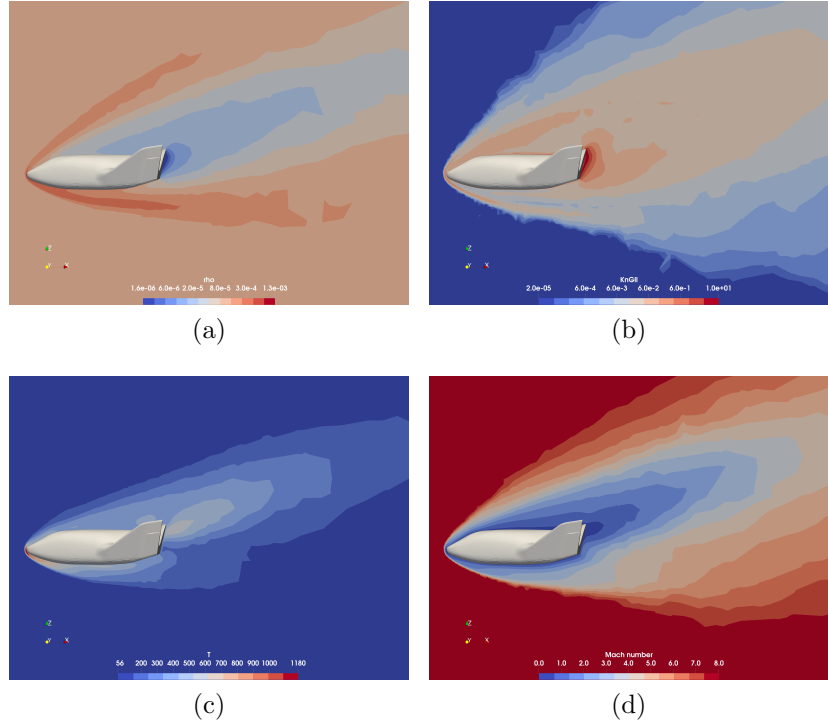


Figure 21: Hypersonic flow around an X38-like space vehicle at $Ma_\infty = 8$ for $Kn_\infty = 0.00275$ by the IAUGKS. Distributions of (a) Density, (b) Kn_{GII} , (c) temperature, and (d) Mach number contours.

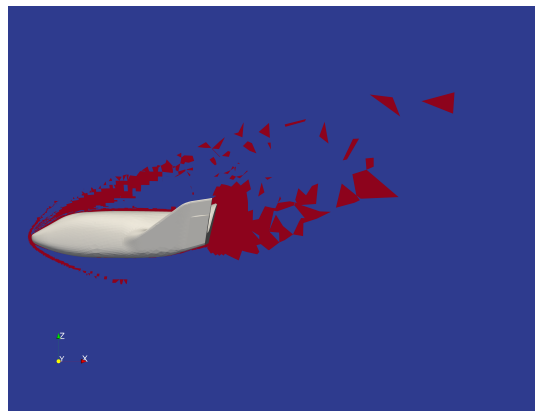


Figure 22: Hypersonic flow around an X38-like space vehicle at $Ma_\infty = 8$ for $Kn_\infty = 0.00275$ by the IAUGKS. Distributions of velocity space adaptation with $C_t = 0.05$ where the DVS (UGKS) is used in 46.37% of this physical domain.

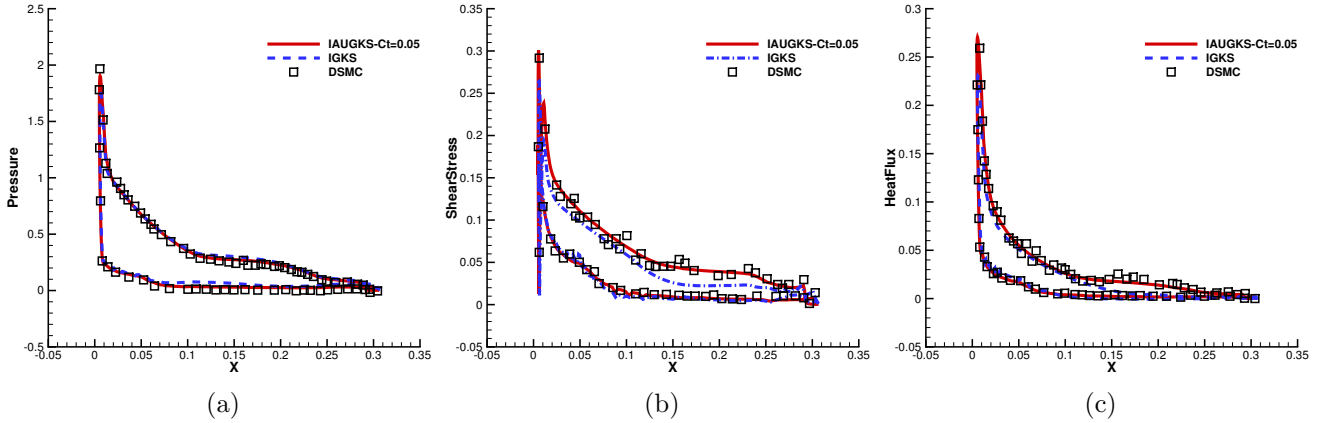


Figure 23: Surface quantities of hypersonic flow around an X38-like space vehicle at $Ma_\infty = 8.0$ for $Kn_\infty = 0.00275$ by the IAUGKS for argon gas compared with the DSMC method and the IGKS. (a) Pressure coefficient, (b) shear stress coefficient, and (c) heat flux coefficient.

3.4. Hypersonic flow over a space station

Hypersonic flow at $Ma_\infty = 25.0$ passing over a space station for $Kn_\infty = 0.01$ is simulated. The characteristic length to define the Knudsen number is selected as the scale of solar panel $L = 0.01$ m. The free stream temperature is $T_\infty = 142.2$ K, and the isothermal wall is applied with $T_w = 500$ K.

The whole physical domain consists of 5,640,776 cells, and the unstructured DVS mesh is discretized into 32,646 cells. In Fig. 24, the DVS mesh is a sphere centered at $0.4 \times (U_\infty, V_\infty, W_\infty)$ with a radius of $42\sqrt{RT_\infty}$. The velocity space is refined in a spherical region near zero velocity point and free stream velocity point with radius $r = 5\sqrt{RT_w}$ and $r = 5\sqrt{RT_\infty}$ respectively.

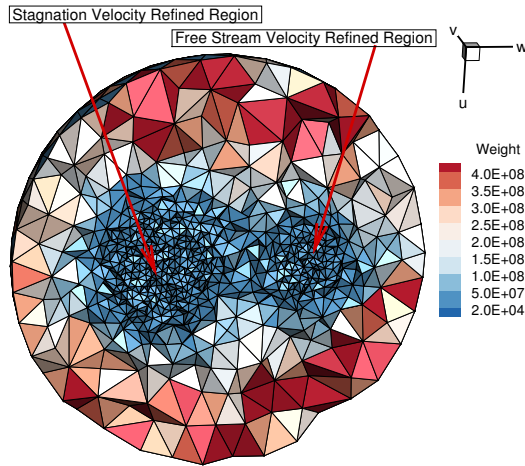


Figure 24: Unstructured DVS mesh with 32,646 cells used for hypersonic flow at $Ma_\infty = 25.0$ and $Kn_\infty = 0.01$ passing over a space station by the IAUGKS.

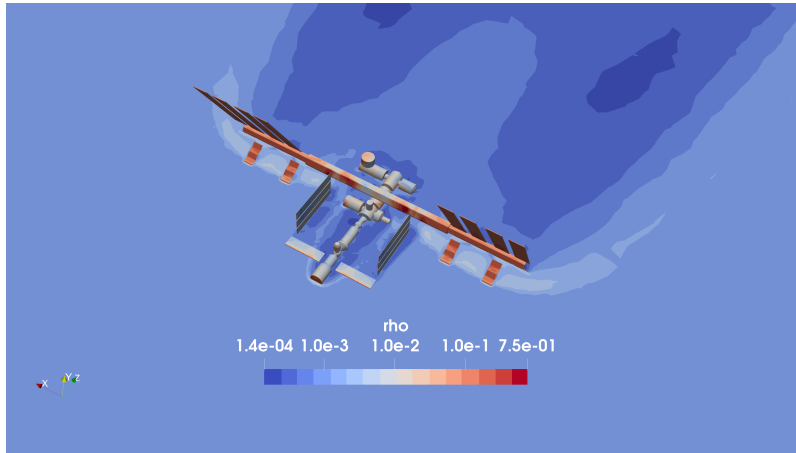
Figure 25 shows the density, Mach number, and temperature contour of hypersonic flow around a space station. As depicted in Fig. 26, the computation region adopting DVS only exists in the close vicinity of the space station, and only occupies 1.53% of the whole domain. As a result, the

demand for CPU cores and memory is greatly reduced. As shown in Table 6, the GSIS, which applies DVS to the whole domain, has to use as many as 9216 cores and 21.5TB to simulate the case, while the IAUGKS only needs 320 cores and less than 2.5TB memory. It is worth noting that the current scheme does not yet account for thermal non-equilibrium, while the GSIS [20] needs handling an additional velocity distribution function, resulting in approximately double the memory consumption and computational cost. If linearly estimate the acceleration rate by considering the core hours, the IAUGKS is more efficient than the GSIS in terms of the computational cost. By implementing better load balancing techniques, it is possible to further reduce both memory consumption and computation time. The physical CFL number is set to 0.4 and the numerical CFL number for implicit iteration is set to 100, and the simulation is conducted on the SUGON computation platform with CPU 7285 32C 2.0GHz.

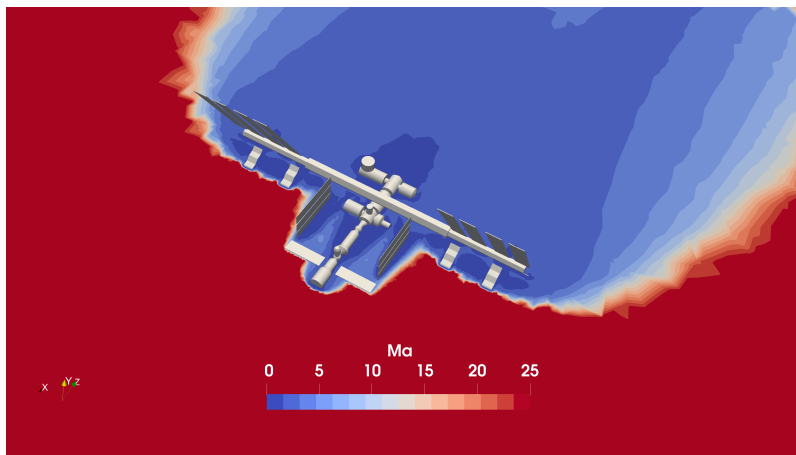
Table 6: Hypersonic flow at $Ma_\infty = 25.0$ passing over a space station for $Kn_\infty = 0.01$ with $C_t = 0.05$. The simulation time and cost are compared with the GSIS.

Method	Cores	Steps	Wall Clock Time, h	Core hours, h	Acceleration Rate
IAUGKS	320	3500 ¹ + 450	11.87	3798.4	2.10
GSIS	9216	4000 + 52	0.867	7990.3	1.0

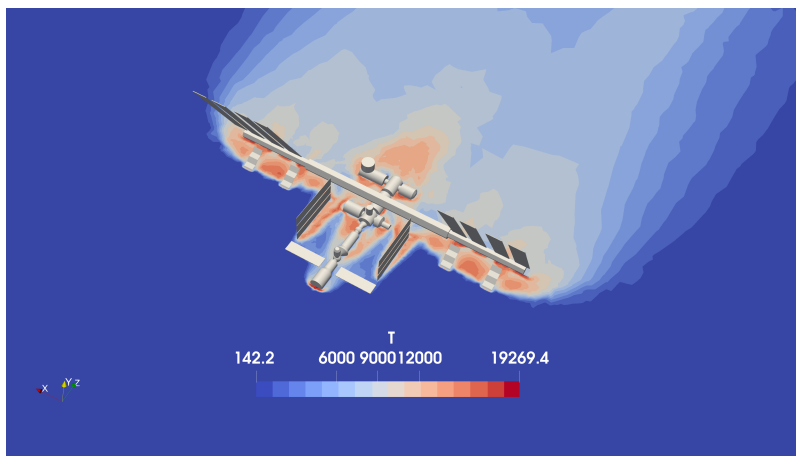
¹ Steps of first-order GKS simulations.



(a)



(b)



(c)

Figure 25: Hypersonic flow around a space station at $Ma_\infty = 25$ for $Kn_\infty = 0.01$. Distributions of (a) density, (b) Mach number, and (c) temperature contours.

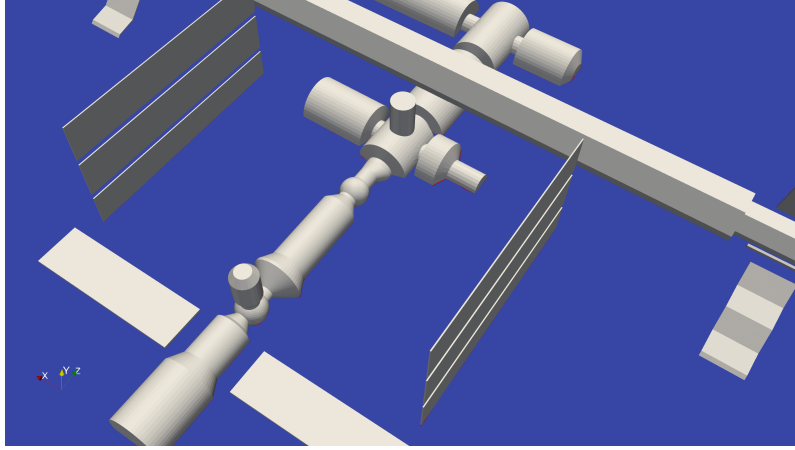


Figure 26: Hypersonic flow at $Kn = 0.01$ and $Ma = 25$ passing over a space station by the IAUGKS. Distributions of velocity space adaptation with $C_t = 0.05$, where the computation domain using DVS takes up 1.53%.

4. Conclusion

In this paper, an implicit adaptive unified gas-kinetic scheme (IAUGKS) for non-equilibrium flow simulation is constructed. Based on the UGKS, a combination of macroscopic implicit prediction and microscopic implicit iteration is adopted, achieving fully implicit and accelerating convergence by 1 to 2 orders of magnitude in all flow regimes. The velocity space adaptation dynamically switches to a continuous distribution function instead of discrete velocity space in the near-continuum flow regime. This automatic dynamic interface between continuous and discrete distribution functions eliminates the need for a buffer zone. Compared to the original UGKS, the IAUGKS demonstrates faster convergence and reduced memory consumption in non-equilibrium flow simulations. In two-dimensional cases, the current scheme exhibits computational efficiency one order of magnitude greater than the UGKWP method, while performing comparably in three-dimensional cases. The velocity space adaptation can save half of the memory in hypersonic flows, utilizing fewer computational resources and simulation time. In summary, the IAUGKS serves as a valuable tool for simulating non-equilibrium flows. The current scheme can be further accelerated by employing techniques such as the multigrid method, GMRES method, and others. Additionally, the IAUGKS provides a solid foundation for multiphysics models and other non-equilibrium flows.

Author's contributions

All authors contributed equally to this work.

Acknowledgments

This work was supported by National Key R&D Program of China (Grant Nos. 2022YFA1004500), National Natural Science Foundation of China (12172316), Hong Kong research grant council (16208021,16301222).

Data Availability

The data that support the findings of this study are available from the corresponding author upon reasonable request.

References

- [1] K. Xu, A unified computational fluid dynamics framework from rarefied to continuum regimes, Cambridge University Press, 2021.
- [2] R. Votta, A. Schettino, A. Bonfiglioli, Hypersonic high altitude aerothermodynamics of a space re-entry vehicle, *Aerospace Science and Technology* 25 (1) (2013) 253–265. doi:10.1016/j.ast.2012.02.001.
- [3] M. S. Ivanov, S. F. Gimelshein, Computational hypersonic rarefied flows, *Annual Review of Fluid Mechanics* 30 (1) (1998) 469–505. doi:10.1146/annurev.fluid.30.1.469.
- [4] G. Bird, Approach to translational equilibrium in a rigid sphere gas, *Physics of Fluids* 6 (10) (1963) 1518–1519.
- [5] G. Bird, Recent advances and current challenges for DSMC, *Computers & Mathematics with Applications* 35 (1-2) (1998) 1–14. doi:10.1016/S0898-1221(97)00254-X.
- [6] J. Fan, C. Shen, Statistical simulation of low-speed rarefied gas flows, *Journal of Computational Physics* 167 (2) (2001) 393–412.
- [7] C. K. Chu, Kinetic-theoretic description of the formation of a shock wave, *The Physics of Fluids* 8 (1) (1965) 12–22. doi:10.1063/1.1761077.
- [8] J. Yang, J. Huang, Rarefied flow computations using nonlinear model Boltzmann equations, *Journal of Computational Physics* 120 (2) (1995) 323–339.
- [9] L. Mieussens, Discrete-velocity models and numerical schemes for the Boltzmann–BGK equation in plane and axisymmetric geometries, *Journal of Computational Physics* 162 (2) (2000) 429–466.
- [10] F. Tcheremissine, Direct numerical solution of the Boltzmann equation, in: *AIP Conference Proceedings*, Vol. 762, American Institute of Physics, 2005, pp. 677–685.
- [11] K. Xu, *Direct modeling for computational fluid dynamics*, World Scientific, 2015. doi:10.1142/9324.
- [12] K. Xu, J. Huang, A unified gas-kinetic scheme for continuum and rarefied flows, *Journal of Computational Physics* 229 (20) (2010) 7747–7764.
- [13] P. L. Bhatnagar, E. P. Gross, M. Krook, A model for collision processes in gases. i. small amplitude processes in charged and neutral one-component systems, *Physical Review* 94 (3) (1954) 511.
- [14] Z. Guo, K. Xu, R. Wang, Discrete unified gas kinetic scheme for all Knudsen number flows: Low-speed isothermal case, *Physical Review E* 88 (3) (2013) 033305. doi:10.1103/PhysRevE.88.033305.
- [15] Z. Guo, K. Xu, Progress of discrete unified gas-kinetic scheme for multiscale flows, *Advances in Aerodynamics* 3 (1) (2021) 6. doi:10.1186/s42774-020-00058-3.

- [16] S. Succi, The lattice Boltzmann equation: for fluid dynamics and beyond, Oxford university press, 2001.
- [17] L. M. Yang, C. Shu, W. M. Yang, Z. Chen, H. Dong, An improved discrete velocity method (DVM) for efficient simulation of flows in all flow regimes, *Physics of Fluids* 30 (6) (2018) 062005. doi:10.1063/1.5039479.
- [18] Z. Y. Yuan, L. M. Yang, C. Shu, K. Jiang, L. Q. Zhang, A variant of improved discrete velocity method for efficient simulation of flows in entire Knudsen number regimes, *Physics of Fluids* 36 (2) (2024) 022018. doi:10.1063/5.0188013.
- [19] W. Su, Y. Zhang, L. Wu, Multiscale simulation of molecular gas flows by the general synthetic iterative scheme, *Computer Methods in Applied Mechanics and Engineering* 373 (2021) 113548. doi:10.1016/j.cma.2020.113548.
- [20] Y. Zhang, J. Zeng, R. Yuan, W. Liu, Q. Li, L. Wu, Efficient parallel solver for high-speed rarefied gas flow using gsis, arXiv preprint arXiv:2310.18916 (2023).
- [21] J. Zeng, W. S. Null, L. Wu, General synthetic iterative scheme for unsteady rarefied gas flows, *Communications in Computational Physics* 34 (1) (2023) 173–207. doi:10.4208/cicp.0A-2023-0068.
- [22] C. Liu, Y. Zhu, K. Xu, Unified gas-kinetic wave-particle methods I: Continuum and rarefied gas flow, *Journal of Computational Physics* 401 (2020) 108977.
- [23] Y. Zhu, C. Liu, C. Zhong, K. Xu, Unified gas-kinetic wave-particle methods. II. Multiscale simulation on unstructured mesh, *Physics of Fluids* 31 (6) (2019) 067105.
- [24] Y. Chen, Y. Zhu, K. Xu, A three-dimensional unified gas-kinetic wave-particle solver for flow computation in all regimes, *Physics of Fluids* 32 (9) (2020) 096108. doi:10.1063/5.0021199.
- [25] W. Long, Y. Wei, K. Xu, Nonequilibrium flow simulations using unified gas-kinetic wave-particle method, *AIAA Journal* 62 (4) (2024) 1411–1433.
- [26] Y. Wei, Y. Zhu, K. Xu, Unified gas-kinetic wave-particle methods VII: Diatomic gas with rotational and vibrational nonequilibrium, *Journal of Computational Physics* 497 (2024) 112610. doi:10.1016/j.jcp.2023.112610.
- [27] C. Liu, K. Xu, Unified gas-kinetic wave-particle methods IV: multi-species gas mixture and plasma transport, *Advances in Aerodynamics* 3 (1) (2021) 9. doi:10.1186/s42774-021-00062-1.
- [28] W. Li, C. Liu, Y. Zhu, J. Zhang, K. Xu, Unified gas-kinetic wave-particle methods III: Multiscale photon transport, *Journal of Computational Physics* 408 (2020) 109280. doi:10.1016/j.jcp.2020.109280.
- [29] X. Yang, W. Shyy, K. Xu, Unified gas-kinetic wave-particle method for gas-particle two-phase flow from dilute to dense solid particle limit, *Physics of Fluids* 34 (2) (2022) 023312. doi:10.1063/5.0081105.

- [30] X. Yang, C. Liu, X. Ji, W. Shyy, K. Xu, Unified gas-kinetic wave-particle methods VI: Disperse dilute gas-particle multiphase flow, *Communications in Computational Physics* 31 (3) (2022) 669–706, arXiv:2107.05075 [physics]. doi:10.4208/cicp.0A-2021-0153.
- [31] X. Yang, Y. Wei, W. Shyy, K. Xu, Unified gas-kinetic wave-particle method for three-dimensional simulation of gas-particle fluidized bed, *Chemical Engineering Journal* 453 (2023) 139541. doi:10.1016/j.cej.2022.139541.
- [32] X. Yang, W. Shyy, K. Xu, Unified gas-kinetic wave-particle method for polydisperse gas-solid particle multiphase flow, *Journal of Fluid Mechanics* 983 (2024) A37. doi:10.1017/jfm.2024.80.
- [33] M. Macrossan, A particle simulation method for the BGK equation, Vol. 585, 2001, p. 426 – 433, cited by: 24. doi:10.1063/1.1407592.
- [34] F. Fei, J. Zhang, J. Li, Z. Liu, A unified stochastic particle Bhatnagar-Gross-Krook method for multiscale gas flows, *Journal of Computational Physics* 400 (2020) 108972. doi:10.1016/j.jcp.2019.108972.
- [35] F. Fei, P. Jenny, A hybrid particle approach based on the unified stochastic particle Bhatnagar-Gross-Krook and DSMC methods, *Journal of Computational Physics* 424 (2021) 109858. doi:10.1016/j.jcp.2020.109858.
- [36] S. Liu, J. Cao, S. Yang, C. Zhong, A multi-scale Boltzmann equation for complex systems of neutral gases across all flow regimes, arXiv preprint arXiv:2406.07038 (2024).
- [37] Y. Zhu, C. Zhong, K. Xu, Implicit unified gas-kinetic scheme for steady state solutions in all flow regimes, *Journal of Computational Physics* 315 (2016) 16–38. doi:10.1016/j.jcp.2016.03.038.
- [38] Y. Zhu, C. Zhong, K. Xu, An implicit unified gas-kinetic scheme for unsteady flow in all Knudsen regimes, *Journal of Computational Physics* 386 (2019) 190–217. doi:10.1016/j.jcp.2019.01.033.
- [39] R. Zhang, S. Liu, J. Chen, C. Zhuo, C. Zhong, A conservative implicit scheme for three-dimensional steady flows of diatomic gases in all flow regimes using unstructured meshes in the physical and velocity spaces, *Physics of Fluids* 36 (1) (2024) 016114. doi:10.1063/5.0186520.
- [40] D. Pan, C. Zhong, C. Zhuo, An implicit discrete unified gas-kinetic scheme for simulations of steady flow in all flow regimes, *Communications in Computational Physics* 25 (5) (2019). doi:10.4208/cicp.0A-2017-0262.
- [41] L. M. Yang, Z. Chen, C. Shu, W. M. Yang, J. Wu, L. Q. Zhang, Improved fully implicit discrete-velocity method for efficient simulation of flows in all flow regimes, *Physical Review E* 98 (6) (2018) 063313. doi:10.1103/PhysRevE.98.063313.
- [42] A.-P. Peng, Z.-H. Li, J.-L. Wu, X.-Y. Jiang, Implicit gas-kinetic unified algorithm based on multi-block docking grid for multi-body reentry flows covering all flow regimes, *Journal of Computational Physics* 327 (2016) 919–942. doi:10.1016/j.jcp.2016.09.050.

- [43] Z. Li, H. Zhang, Study on gas kinetic unified algorithm for flows from rarefied transition to continuum, *Journal of Computational Physics* 193 (2) (2004) 708–738.
- [44] Z. Li, A. Peng, Q. Ma, L. Dang, X. Tang, X. Sun, Gas-kinetic unified algorithm for computable modeling of Boltzmann equation and application to aerothermodynamics for falling disintegration of uncontrolled Tiangong-No. 1 spacecraft, *Advances in Aerodynamics* 1 (1) (2019) 1–21.
- [45] R. Yuan, C. Zhong, A conservative implicit scheme for steady state solutions of diatomic gas flow in all flow regimes, *Computer Physics Communications* 247 (2020) 106972. doi:10.1016/j.cpc.2019.106972.
- [46] T. Xiao, C. Liu, K. Xu, Q. Cai, A velocity-space adaptive unified gas kinetic scheme for continuum and rarefied flows, *Journal of Computational Physics* 415 (2020) 109535. doi:10.1016/j.jcp.2020.109535.
- [47] Y. Wei, W. Long, K. Xu, Adaptive unified gas-kinetic scheme for diatomic gases with rotational and vibrational nonequilibrium, arXiv:2312.02449 [physics] (Dec. 2023).
- [48] L. M. Yang, L. C. Han, H. Ding, Z. H. Li, C. Shu, Y. Y. Liu, Adaptive partitioning-based discrete unified gas kinetic scheme for flows in all flow regimes, *Advances in Aerodynamics* 5 (1) (2023) 15. doi:10.1186/s42774-023-00142-4.
- [49] Y. Wei, J. Cao, X. Ji, K. Xu, Adaptive wave-particle decomposition in UGKWP method for high-speed flow simulations, *Advances in Aerodynamics* 5 (1) (2023) 25.
- [50] K. Xu, A gas-kinetic BGK scheme for the Navier–Stokes equations and its connection with artificial dissipation and Godunov method, *Journal of Computational Physics* 171 (1) (2001) 289–335.
- [51] J. Wendt, Drag coefficients of spheres in hypersonic non-continuum flow, Final Scientific Report, Contract F61052-69-C-0024, AFCRL 30 (1971).
- [52] D. Jiang, M. Mao, J. Li, X. Deng, An implicit parallel UGKS solver for flows covering various regimes, *Advances in Aerodynamics* 1 (1) (2019) 1–24.